Recurrent High-Resolution Satellite Observations Quantify Facility-Resolved Annual Large-Emitter Methane Emissions in the Permian Basin

Dylan Jervis[1], Alessandro Ambler[1], Simon Andersson-Bastable[1], Amanda Delgado-Recke[1], Victoria Foing[1], Jack Hayden[1], Krishna Mooroogen[1], Jason McKeever[1], Frederic Piedboeuf[1], Antoine Ramier[1], and Mathias Strupler[1]*

[1]GHGSat Inc, 1130 Sherbrooke Street West, Montreal, QC, Canada, H3A 2M8
*Email: dylan.jervis@ghgsat.com

KEYWORDS: Methane, oil and gas, remote sensing, annual emissions

SYNOPSIS: A framework for estimating facility-resolved annual methane emissions from repeated sampling and per-observation detection probabilities.

ABSTRACT:

Repeated high-resolution satellite observations can identify large methane emissions from individual oil and gas facilities, but sparse sampling, intermittent emissions, and variable observation conditions complicate the estimation of annual facility-level emissions. We develop an empirical hierarchical Bayesian method to estimate facility-resolved annual large-emitter methane emissions, with uncertainty, from repeated satellite plume detections and non-detections that were attributed to individual facilities. We apply the method to approximately 100,000 upstream and midstream facilities in the Permian Basin observed by the GHGSat satellite constellation from 2023 through 2025.

Mean annual large-emitter emission rates differed strongly by facility class, averaging approximately 0.46 kg h^{-1} for wells, 32–36 kg h^{-1} for compressor/gathering stations, and 139–144 kg h^{-1} for gas processing plants. Mean large-emitter persistence was approximately 0.001 for wells, 0.089–0.091 for compressor/gathering stations, and 0.238–0.249 for gas processing plants. Facility-level estimates were moderately heavy-tailed, with approximately 30–35% of midstream facilities accounting for 50% of estimated annual large-emitter emissions. Class-level mean estimates varied little between years, and more than 98% of matched midstream facilities showed no interannual change exceeding the combined estimation uncertainty. Summed and extrapolated facility estimates for the considered facility classes

yielded GHGSat-derived Permian Basin totals of 1.70, 1.66, and 1.63 Mt y^{-1} for 2023, 2024, and 2025, respectively.

These results demonstrate that recurrent satellite observations can support facility-resolved, uncertainty-quantified estimates of the annual contribution from large methane emission events. The framework complements ground and aerial measurements, regional atmospheric inversions, and bottom-up inventories by providing repeated, attributable measurements across large facility populations.

INTRODUCTION

Methane is the second-largest contributor to anthropogenic global warming after CO_2[1]. Because most methane emissions arise from human activities, and because methane has a relatively short atmospheric lifetime and substantial near-term mitigation potential, reducing anthropogenic methane has become a major climate priority. The oil and gas (O&G) sector contributes more than 20% of anthropogenic methane emissions [2] and is therefore an important focus for near-term mitigation. Measurement-informed estimates at the facility scale are particularly valuable because they support source attribution and help identify where mitigation efforts can be most effectively targeted.

High-resolution satellite methane observations are increasingly being incorporated into operational monitoring and mitigation frameworks. For example, the U.S. EPA Super Emitter Program[3] uses approved remote-sensing observations to identify large methane emission events and notify operators, while UNEP's Methane Alert and Response System[4] uses satellite observations to support mitigation outreach. Oil and gas operators also increasingly use commercial satellite observations to identify and quantify methane emissions. These applications demonstrate the growing operational value of facility-attributed satellite observations, but individual plume detections do not alone provide temporally representative emission estimates at annual inventory and reporting timescales.

Repeated observations of individual facilities provide a means to move beyond event-level plume detections toward temporally-averaged estimates of facility emissions. Such measurement-informed estimates are pertinent to reporting frameworks such as the Oil and Gas Methane Partnership (OGMP) 2.0[5], which emphasizes reconciliation between source-level inventories and independent site-level measurements. Recurrent satellite observations therefore offer a pathway to support measurement-informed reporting and reconciliation at scale, particularly for large, intermittent emissions that may be underrepresented in bottom-up inventories or measurement programs with limited temporal coverage. However, converting repeated satellite observations into temporally representative facility estimates is non-trivial because each overpass samples only a snapshot of the emission state under observation-specific detection conditions.

Recent measurement-based studies have demonstrated the value of large-scale aerial and satellite observations for improving oil and gas methane inventories[6–9]. Aircraft campaigns have used facility- and source-resolved detections to estimate regional, basin-scale, operator-scale, or facility-class emissions, often by combining detected emissions with statistical extrapolation or models for emissions below the measurement detection limit[6–8]. However, because aircraft site revisits are typically temporally clustered within days and/or weeks, such surveys are less well suited to estimating temporally averaged emissions from individual facilities over annual timescales. Recent cause-resolved aerial measurements found significant temporal and inter-operator variation in emissions and noted that temporally concentrated operational practices can bias annualized inventories derived from short measurement campaigns[10].

Satellite studies provide complementary strengths. Although satellite instruments are generally less sensitive than many aircraft- and ground-based measurement systems, they can provide repeated, temporally-distributed observations across large producing regions. This spatiotemporal coverage advantage makes satellite data particularly valuable for observing rare, high-emission-rate events that contribute disproportionately to total emissions but can be missed by spatially limited ground networks or spatially and temporally concentrated aircraft campaigns. High-resolution point-source imagers can attribute large methane plumes to individual facilities and estimate emissions from blowout events[11–13] or, when observations are repeated, estimate annual emissions[9] and observation persistence[9,14], while moderate-resolution measurements can map super-emitters[15] and estimate basin-scale emissions and sub-regional methane intensities[16]. However, facility-resolved satellite estimates have generally focused on detected emitting sites, individual emission events, persistence statistics, or aggregated sector-wide emissions. Less attention has been given to estimating annual emissions for all observed facilities - including those without plume detections - while explicitly accounting for observation-specific detection probability.

Here, we develop a detection-probability-aware method for estimating annual methane emissions from individual oil and gas facilities using repeated satellite detections and non-detections. The method combines facility-specific observation histories with a population-informed prior derived from measurements of similar facilities, allowing annual emissions to be estimated even when facility observation histories are sparse or contain no plume detections. The resulting estimates represent the annual mean contribution from emissions above the satellite-detectable rates considered here (approximately ≥ 50 kg h^{-1}) and provide facility-resolved estimates suitable for comparison with bottom-up inventories and measurement-informed reconciliation frameworks such as OGMP 2.0.

MATERIALS AND METHODS

2.1. Facility-resolved satellite observation data

We constructed facility-level methane observation histories by attributing GHGSat plume detections and clear-sky non-detections to mapped facility footprints. The spatial origin of each detected plume was estimated using a machine-learning model (see Section S1). Facility footprints were identified using Sentinel-2 imagery and grouped into classes representing broadly similar infrastructure and emission behavior, including gas processing plants, compressor/gathering stations, and well sites (see Section S2). Detected plumes were then assigned probabilistically to candidate facilities using an area-normalized overlap integral between the plume-origin probability distribution and the mapped facility footprints (see Section S3). Importantly, these facility methane observation histories are constructed for all GHGSat-observed facilities, irrespective of whether a plume was detected. For each facility and calendar year, the resulting observation history contained all clear-sky observations, the detection outcome for each observation, the quantified emission rate for detected plumes, and an observation-specific probability-of-detection function. For a facility with n observations at times $\mathbf{t} = \{t_1, t_2, \ldots, t_n\}$, we denote the detection outcomes by

$$\mathbf{d} = \{d_1, d_2, \ldots, d_n\}, \tag{1}$$

where $d_i = 1$ indicates a detected plume and $d_i = 0$ indicates a non-detection. The corresponding retrieved emission rates for detected plumes are denoted by

$$\mathbf{q} = \{q_i : d_i = 1\}. \tag{2}$$

Non-detections do not provide measured emission rates and are therefore represented by the detection Boolean rather than interpreted as $q_i = 0$. Each observation has an associated probability-of-detection function,

$$\mathrm{POD}_i(Q; u_i, \delta\Omega_i), \tag{3}$$

which estimates the probability of detecting a plume with true emission rate Q under the conditions of observation i. The function depends on the local wind speed u_i and methane column-density retrieval precision $\delta\Omega_i$ (see section S4).

2.2. Discretized facility emission model

We represent the instantaneous emission state of each facility using a site-specific emission-rate distribution, $\rho(Q)$, containing an explicit probability mass at $Q = 0$. The zero-emission state represents periods without emissions in the large-emitter range considered in this study. Rather than assuming a functional form for $\rho(Q)$ as in Ref[17], we discretized the distribution over $K + 1$ emission states with representative rates $\{Q_0, Q_1, \dots, Q_K\}$ with $Q_0 = 0$. The representative emission rate $Q_k = (b_k - a_k)/\log(\frac{b_k}{a_k})$ was defined as the log-uniform bin mean of the lower a_k and upper b_k edges of emission-rate bin k. Let $\mathbf{p} = \{p_0, p_1, \dots, p_K\}$ denote the corresponding probability masses with the normalization condition $\sum_{k=0}^{K} p_k = 1$. The vector $\mathbf{p}$ defines a multinomial distribution over the discrete facility emission state. Here, p_0 is the probability that the facility is in the zero large-emission state, and p_k, for $k \geq 1$, is the probability that its emission rate lies in positive emission-rate bin k. This discrete representation accommodates broad and skewed facility emission-rate distributions without imposing a potentially misspecified functional form at the individual-facility level.

2.3. Detection-Aware Likelihood

For observation i, the probability of detecting an emission from emission rate bin k is

$$\widehat{\mathrm{POD}}_{ik} = \int \mathrm{POD}_i(Q_k; u, \delta\Omega_i)\, f_u(u \mid u_i)\, du, \tag{4}$$

where $f_u(u \mid u_i)$ is the uncertainty distribution for the wind speed associated with observation i.
The model-predicted probability of obtaining any detection during observation i is therefore

$$m_i(\mathbf{p}) = \sum_{k=1}^{K} p_k\, \widehat{\mathrm{POD}}_{ik}. \tag{5}$$

The summation begins at $k = 1$ because the probability of detecting the zero-emission state is zero.
For a detected plume, the likelihood must account for both the probability that the facility occupied a given emission state and the likelihood of obtaining the retrieved emission rate from that state. We define R_{ik} as the joint detection-and-retrieval likelihood density, marginalized over wind-speed uncertainty and conditional on emission state k:

$$R_{ik} = \int \mathrm{POD}_i(Q_k; u, \delta\Omega_i)\, f_q(q_i \mid Q_k, u)\, f_u(u \mid u_i)\, du, \tag{6}$$

where $f_q(q_i \mid Q_k, u)$ is the probability density of retrieving emission rate q_i, conditional on true emission rate Q_k and wind speed u. Details of the wind-speed and emission-rate uncertainty models are provided in Section S5.

The likelihood contribution from a detected plume is $\sum_{k=1}^{K} p_k\, R_{ik}$, whereas the likelihood contribution from a non-detection is $1 - m_i(\mathbf{p})$. The log-likelihood for the observation history of a facility within a specified time period is therefore

$$\log L(\mathbf{p} \mid \mathbf{q}, \mathbf{d}) = \sum_{i:d_i=1} \log\left(\sum_{k=1}^{K} p_k\, R_{ik}\right) + \sum_{i:d_i=0} \log\left[1 - m_i(\mathbf{p})\right]. \tag{7}$$

This formulation accounts for two possible causes of a non-detection: the facility may have occupied the zero large-emission state, or it may have emitted at a positive rate that was not detected given the per-observation detection probability. Non-detections are therefore not strictly interpreted as observations of zero emissions.

2.4. Empirical hierarchical prior

Individual facilities commonly have too few observations to constrain all emission-state probabilities independently. We therefore used an empirical hierarchical prior that pooled information among facilities in the same facility class: wells, compressor/gathering stations, and gas processing plants. For facility j belonging to class g, the vector of emission-state probabilities was assigned a Dirichlet prior which is the conjugate prior of a multinomial distribution[18]:

$$\mathbf{p}_j = \mathrm{Dirichlet}(\boldsymbol{\alpha}_g) = \frac{1}{\mathrm{B}(\boldsymbol{\alpha}_g)} \prod\nolimits_k p_k^{\alpha_{g;k}-1} \tag{8}$$

With $\mathrm{B}(\boldsymbol{\alpha}_g)$ a normalization constant (a multivariate Beta function) and the concentration parameters defined as

$$\alpha_{g;k} = 1 + \lambda_g\, \bar{p}_{g;k}. \tag{9}$$

Here, $\bar{\mathbf{p}}_g$ is the empirical emission-state distribution for class g, and λ_g is a concentration parameter controlling the influence of the prior. The additive unit term provides a uniform baseline contribution to each emission state to aid the estimation procedure.

We estimated $\bar{\mathbf{p}}_g$ empirically from the pooled observation 2023-2025 histories of facilities in class g. Let N_g denote the total number of valid observations and let D_{gk} denote the set of detected plumes assigned to positive emission-rate bin k. Similar in general conception to Refs[8,19], each detected plume was weighted by the inverse of its observation-specific probability of detection, giving the detection-corrected effective count in bin k as

$$\widetilde{D}_{g;k} = \sum_{j \in D_{g;k}} \frac{1}{\widehat{\mathrm{POD}}_{jk}}, \tag{10}$$

with the effective count in the zero emission-rate bin defined as $\widetilde{D}_{g;0} = N_g - \sum_{k=1} \widetilde{D}_{g;k}$. The prior mean emission rate distribution is then

$$\bar{p}_{g;k} = \frac{\widetilde{D}_{g;k}}{N_g} \tag{11}$$

and we note that we can estimate the prior mean persistence using the $k = 0$ bin as $\bar{\pi}_g = 1 - \bar{p}_{g;0}$. The prior emission-rate distributions for the three facility classes are shown in Figure 1a.

We estimated the concentration parameter λ_g by matching the empirical between-facility variance in each emission state to the corresponding Dirichlet marginal variance (see Section S7 for more details). Larger values of λ_g constrain facility-level distributions more strongly toward the class mean, whereas smaller values allow the facility-specific observations to exert greater influence.

2.5. Posterior Sampling and Facility Emission-Rate Estimates

For each facility-year, the posterior distribution of the emission-state probability vector was proportional to the product of the detection-aware likelihood and the Dirichlet prior. Ignoring terms that do not depend on the facility emission-state probabilities, the log posterior was

$$\log P(\mathbf{p}_j \mid \mathbf{q}_j, \mathbf{d}_j) = \log L(\mathbf{p}_j \mid \mathbf{q}_j, \mathbf{d}_j) + \sum_{k=0}^{K} (\alpha_{gk} - 1) \log p_{jk}. \tag{12}$$

We sampled this posterior using a Metropolis-Hastings Markov chain Monte Carlo algorithm (see section S6 for more details).

For retained posterior draw r, the temporally averaged large-emitter emission rate for facility j was

$$Q_j^{(r)} = \sum_{k=0}^{K} p_{jk}^{(r)} Q_k, \tag{13}$$

where $Q_0 = 0$ and Q_k is the representative emission rate for positive emission state k. The facility-level point estimate was the posterior mean

$$\overline{Q}_j = \frac{1}{R} \sum_{r=1}^{R} Q_j^{(r)}, \tag{14}$$

where R is the total number of retained posterior draws across chains. The 2.5th and 97.5th percentiles of the sampled Q_j values were reported as the 95% credible interval.

Sampling performance was monitored using the mean proposal acceptance rate across chains. Facility-year fits with acceptance rates outside the range 0.10-0.60 were treated as unreliable. For these cases, and for facilities with only a single non-detection, the class-level prior mean was reported instead and no facility-specific credible interval was assigned.

Large-emitter persistence was also calculated from each retained posterior draw as

$$\pi_j^{(r)} = 1 - p_{j0}^{(r)} = \sum_{k=1}^{K} p_{jk}^{(r)} \tag{15}$$

where $p_{j0}^{(r)}$ is the posterior probability that facility j occupied the zero large-emission state. The posterior mean of π_j was reported as the facility-level persistence estimate. Class-level persistence was calculated as the mean facility persistence within each facility class. Note that this quantity describes the fraction of time a facility occupies an emission state within the large-emitter range considered here and should not be interpreted as the fraction of time the facility emits methane at any rate.

RESULTS AND DISCUSSION

3.1. Class-level Prior Distributions and Example Facility Time Series

The class-level prior emission-state distributions, $\bar{p}_{g;k}$, are shown in Figure 1a for wells, compressor/gathering stations, and gas processing plants. When comparing the relative magnitude of probability masses in the positive emission rate bins between facility classes, we can see that gas processing plants are the most persistent emitters, followed by compressor/gathering stations, and finally wells (corroborated by the fact that wells had the highest probability in the $Q = 0$ bin among the facility classes and gas processing plants the lowest). The large emission rate tails of the distribution for all facility classes are power-law like, consistent with previous studies[17,20,21]. Towards smaller emission-rate bins, a local maximum is evident. This feature may reflect residual detection probability bias near the lower end of the observable range, although it could also arise from the true shape of the facility-class emission-rate distribution.

The class-level prior mean emission rate was calculated as $\bar{Q}_g = \sum_{k=0}^{K} \bar{p}_{g;k}\, Q_k$. Across 2023-2025, the resulting prior mean [95% bootstrap interval] large-emitter emission rates were 0.46 [0.40, 0.53] kg h^{-1} for wells, 32.3 [26.1, 40.7] kg h^{-1} for compressor/gathering stations, and 141.6 [92.5, 194.9] kg h^{-1} for gas processing plants. The corresponding prior mean [95% bootstrap interval] large-emitter persistence values were calculated as $\bar{\pi}_g = 1 - p_0$ and were 0.0012 [0.0010, 0.0015] for wells, 0.095 [0.068, 0.124] for compressor/gathering stations, and 0.261 [0.152, 0.393] for gas processing plants.

Figures 1b and 1c illustrate how facility-specific observation histories update these class-level priors. Figure 1b shows a gas processing plant observed in 2025 with both plume detections and non-detections. Detected plumes are shown with their estimated instantaneous emission rates and associated uncertainties. Non-detections are plotted at $q = 0$. The vertical grayscale bars show the observation-specific probability of detection as a function of emission rate, with darker shading indicating emission rates that were less likely to be detected under the conditions (retrieval precision and wind speed) of that particular observation. The horizontal red line in Figure 1b shows the posterior mean annual large-emitter emission rate for the facility, and the shaded red band shows the 95% credible interval. The estimated mean emission rate for the example facility in Figure 1b was 768.6 (+500.8/-363.3) kg h^{-1}, and the estimated large-emitter persistence was 0.69. Both of these estimates were higher than the corresponding gas-processing-plant prior values, reflecting the influence of the detected plumes in the facility observation history.

Figure 1c shows a compressor/gathering station for which all valid clear-sky observations in 2025 were non-detections. The method nevertheless produces a nonzero posterior estimate because a non-detection does not imply zero emissions and because the class-level prior assigns some probability to positive emission states. The estimated annual large-emitter emission rate was 11.5 (+41.2/-11.4) kg h^{-1}, and the estimated persistence was 0.07, both below the corresponding compressor/gathering prior values. For facilities with only non-detections, the annual emission estimate depends strongly on observation sensitivity. A non-detection obtained under conditions with a high probability of detecting low emission rates provides stronger evidence against positive large-emission states than a non-detection obtained under less favorable detection conditions. Repeated sensitive non-detections therefore shift the posterior toward lower emission rates and lower persistence.

Because large-emitter persistence for wells was very low, most individual well observation histories contained insufficient information for reliable facility-specific estimation. We therefore report the class-level prior mean emission rate and persistence for wells rather than well-specific posterior estimates.

3.2. Annual Mean Large-Emitter Facility Emission Estimates

Figure 2 shows estimated annual large-emitter methane emissions from facilities in the Permian Basin in 2023, 2024, and 2025. Marker size indicates the magnitude of the annual emission estimate, while marker colour indicates facility type: blue for wells, orange for compressor/gathering facilities, and green for gas-processing plants. The mapped spatial distribution reflects both the underlying geography of oil and gas infrastructure and the spatial coverage of GHGSat observations. The broad western cluster of facility emission estimates corresponds to the Delaware Basin, whereas the more eastern cluster corresponds to the Midland Basin, the Permian Basin's two principal producing sub-basins. A similar two-lobed spatial emissions pattern has been observed in coarser-resolution TROPOMI emission inversions[22,23].

Table 1 summarizes the estimated annual large-emitter emissions for Permian Basin facilities from 2023 through 2025. Mean observation frequency increased over the study period, from 4.1 to 6.4 observations per well, 5.0 to 8.5 observations per compressor/gathering station, and 4.3 to 6.9 observations per gas processing plant. Across facility classes and years, the 2.5th–97.5th percentile range in observation counts extended from one observation per facility to as many as 21 observations for compressor/gathering stations and 18 observations for gas processing plants.

The estimated mean annual large-emitter emission rate for wells was 0.46 kg h^{-1} in each year, based on the class-level prior mentioned previously because facility-specific well estimates were not reported. Mean estimates for compressor/gathering stations varied only modestly, from 35.9 kg h^{-1} in 2023 to 32.2 kg h^{-1} in 2025, while mean estimates for gas processing plants remained within a range of 139.7–144.3 kg h^{-1}. This limited interannual variability is consistent with regional emissions estimates derived from TROPOMI observations, which showed little change in total Permian Basin emissions between 2019 and the end of 2023[22]. Our facility-class estimates were approximately 50-65% of those reported by a 2024 aerial LiDAR inventory[8], which estimated mean annual emission rates of approximately 1 kg h^{-1} for wells, 60 kg h^{-1} for compressor/gathering facilities, and 230 kg h^{-1} for gas processing plants. This difference is likely driven by the lower detection threshold of the aerial LiDAR versus satellite measurements[24–26]. The satellite-derived values therefore represent the annual contribution from comparatively large, satellite-observable emission events, whereas the aerial inventory captures a greater contribution from smaller emissions though may be less likely to observe rare large-emission events due to their more limited spatiotemporal coverage.

Facility-level estimates varied widely within both midstream facility classes: the 2.5th–97.5th percentile range was 14.9–97.4 kg h^{-1} for compressor/gathering stations across the three years and 52.0-412.5 kg h^{-1} for gas processing plants. Figure 3a shows the distribution of annual emission estimates. The distributions were skewed to larger emission rates, with extended high-emission tails, and had similar shapes across the three years, consistent with the limited interannual variability in the class-level means reported in Table 1. Figure 3b shows the same estimates as cumulative emission distribution curves, with facilities ranked from highest to lowest annual mean emission rate. Approximately 30–35% of facilities accounted for 50% of the estimated annual large-emitter emissions in both facility classes. For context, instantaneous oil-gas emission-event distributions measured by satellite systems were found to be much more skewed[17,20,21]. For example, a truncated power-law distribution proportional to $q^{-2.3}$ between 50 and 100,000 kg h^{-1} implies that approximately 8% of emission events contribute to 50% of the detected emission-rate total. This difference reflects the different levels of aggregation represented by the two distributions: an event-level distribution characterizes the rates of individual emissions at the times they occur, whereas the distributions in Figures 3a and b characterize facility-level annual means that average across emitting and non-emitting periods. Therefore, temporal averaging, repeated sampling, and the Bayesian estimation framework appear to reduce the skewness of the facility-level annual estimates relative to the underlying instantaneous event distribution.

3.3. GHGSat-Derived Emission Totals

Table 2 summarizes the number of observed and mapped facilities, as well as emission totals per facility class. The number of GHGSat satellite-observed facilities ranged from 76,117 to 101,408 wells, 1,320 to 1,584 compressor/gathering stations, and 112 to 132 gas processing plants per year, whereas the total number of mapped facilities was approximately 1.4-2.3x higher: 173,840 wells, 2,417 compressor/gathering stations, and 189 gas processing plants. Summing the facility-level estimates yields a GHGSat satellite-observed Permian total means [95% bootstrap intervals] of 0.862 [0.807, 0.926] Mt y^{-1} in 2023, 1.040 [0.974, 1.105] Mt y^{-1} in 2024, and 0.995 [0.937, 1.057] Mt y^{-1} in 2025. We classify this as a partial total given that it only includes wells, compressor/gathering stations, and gas processing plants observed by GHGSat at least once during the corresponding year.

However, if we scale by the total number of mapped wells, compressor/gathering stations, and gas processing plants in the Permian - both observed and unobserved by GHGSat - we can extrapolate to total means [95% bootstrap intervals] of 1.70 [1.58, 1.83] Mt y^{-1} in 2023, 1.66 [1.56, 1.77] Mt y^{-1} in 2024, and 1.63 [1.52, 1.74] Mt y^{-1} in 2025. The GHGSat extrapolated totals exclude facility classes outside the scope of the study, such as transmission pipelines, and emissions below the satellite-observable range. For context, previous basin-wide measurement-based estimates include 2.9 Mt y^{-1} from TROPOMI for the 2018–2020 study period[27], 4.0 ± 1.1 Mt y^{-1} from TROPOMI for 2019–2023[22], approximately 3.6 Mt y^{-1} from MethaneSAT observations[16] in 2024 and 2025, and 5.13 Mt y^{-1} from a 2024 aerial LiDAR inventory that included gathering pipelines and modeled subthreshold emissions[8]. Therefore, the extrapolated GHGSat totals represent approximately between 32% and 59% of these basin-wide estimates and should be interpreted as estimates of the annual contribution from large, satellite-observable emissions for the included facilities, rather than as complete Permian Basin methane inventories. Differences in study period and facility class definition also limit direct comparison between the GHGSat and previous estimates.

3.4. Large-Emitter Persistence

In Figure 3c, we show that the mean estimated large-emitter persistence was approximately 0.089 – 0.091 for compressor/gathering stations and approximately 0.238–0.249 for gas processing plants. Facility-level persistence also varied substantially, with 2.5th–97.5th percentile ranges of approximately

0.061–0.189 for compressor/gathering stations and 0.110–0.552 for gas processing plants. The well emission-rate and persistence values were derived from the class-level prior and therefore do not have corresponding facility-level percentile ranges.

For context, a temporally concentrated aircraft campaign[28] reported a mean persistence of 0.26 for strong Permian Basin point sources detected at least once and observed on at least three overflights. This value is similar to the persistence estimated here for midstream facilities, but the estimates are not directly comparable: the aircraft estimate combined multiple oil and gas sectors, was conditioned on detected sources, and defined persistence as the fraction of overflights with a plume detection without explicitly accounting for observation-specific detection probability. A global satellite analysis similarly reported a persistence of 0.15 for detected oil and gas sources[9], also for sites with at least one plume detection. In contrast, our estimates apply to the full mapped facility populations within each class and account for the probability that a positive large-emission state may not be detected.

3.5. Interannual Changes in Facility Emission Estimates

To assess interannual variability in estimated facility-level emission rates, we compared posterior mean emission-rate estimates between consecutive years for facilities with estimates in both years. Each panel in Figure 4 shows the estimated mean emission rate in year $y+1$ versus year y, with points falling on the 1:1 line indicating unchanged facility estimates between years. To determine whether observed changes are statistically meaningful given the estimation uncertainty, we compute a z-score for each facility (under an assumption of normally distributed per-facility estimates, an assumption that is admittedly approximate): $z = (\bar{Q}_{y+1} - \bar{Q}_y)/\sqrt{\sigma_y^2 + \sigma_{y+1}^2}$, where $\sigma \approx (Q_{97.5} - Q_{2.5})/3.92$ is the posterior standard deviation estimated from the 95% credible interval. Facilities with $|z| > 1.96$, corresponding to the two-sided 95% threshold of the standard normal distribution, were classified as having an interannual change that exceeded the combined estimation uncertainty at the 95% confidence level. Point shading quantifies the $|z|$ value, with darker colors indicating more statistically significant changes.

For compressor/gathering stations, 948 facilities were matched between 2023 and 2024 and 1,046 between 2024 and 2025. Of these, 99.6% and 99.8%, respectively, had $|z| \leq 1.96$, corresponding to only four and two facilities with changes exceeding the combined uncertainty. For gas processing plants, 64 facilities were matched between 2023 and 2024 and 65 between 2024 and 2025; 98.4% and 98.5%, respectively, had ($|z| \leq 1.96$), corresponding to one facility in each comparison with a change exceeding the combined uncertainty. Thus, for nearly all matched facilities, any estimated year-to-year differences were small relative to the uncertainty in the annual facility estimates.

In summary, this study demonstrates that repeated high-resolution satellite observations can be converted from a collection of plume detections and non-detections into facility-resolved estimates (with uncertainty) of annual large-emitter methane emissions and persistence. By explicitly accounting for observation-specific detection probability and including prior information from similar facilities, the framework provides estimates even when individual observation histories are sparse. Moreover, the framework allows the potential for observations from instruments with substantially different detection sensitivities (though similar spatial resolutions, given that the emission rate distribution is spatial resolution dependent[8,17,29]) to be used alongside each other to estimate emissions. Applied to the Permian Basin, the method revealed strong differences among facility classes, substantial heterogeneity within midstream classes, and limited interannual variability in both class-level means and the vast majority of individual facility estimates. The resulting aggregate annual facility emission rate totals represent only the contribution from large, satellite-observable emissions for the facility classes included in the analysis and should not be interpreted as complete basin inventories. Rather, they provide a complementary measurement-informed component with facility-scale spatial attribution and repeated temporal sampling. Combined with lower-threshold aerial surveys, regional atmospheric inversions, and bottom-up source estimates, this approach can improve reconciliation across measurement scales, identify facilities that contribute disproportionately to large-emitter totals, and support monitoring and mitigation efforts at actionable facility scale.

SUPPORTING INFORMATION

Additional description of the plume origin estimation method (Text S1), the facility detector (Text S2; Fig. S1), the plume-facility attribution model (Text S3), the per-observation probability of detection (Text S4), the instantaneous plume emission rate and uncertainty parametrization (Text S5), the posterior sampling method (Text S6), the Dirichlet concentration parameter estimation (Text S7), and the estimation precision (Text S8, Fig S2).

CORRESPONDING AUTHOR

Dylan Jervis
GHGSat Inc, 1130 Sherbrooke Street West, Montreal, Quebec, Canada, H3A 2M8
Email: dylan.jervis@ghgsat.com
orcid.org/0009-0009-5387-635X

AUTHORS

Alessandro Ambler
GHGSat Inc, 1130 Sherbrooke Street West, Montreal, Quebec, Canada, H3A 2M8
Email: alessandro.ambler@mail.mcgill.ca

Simon Andersson-Bastable
GHGSat Inc, 1130 Sherbrooke Street West, Montreal, Quebec, Canada, H3A 2M8
Email: sandersson@ghgsat.com

Amanda Delgado-Recke
GHGSat Inc, 1130 Sherbrooke Street West, Montreal, Quebec, Canada, H3A 2M8
Email: arecke@ghgsat.com

Victoria Foing
GHGSat Inc, 1130 Sherbrooke Street West, Montreal, Quebec, Canada, H3A 2M8
Email: vfoing@ghgsat.com

Jack Hayden
GHGSat Inc, 1130 Sherbrooke Street West, Montreal, Quebec, Canada, H3A 2M8
Email: jhayden@ghgsat.com

Krishna Mooroogen
GHGSat Inc, 1130 Sherbrooke Street West, Montreal, Quebec, Canada, H3A 2M8
Email: kmooroogen@ghgsat.com

Jason McKeever
GHGSat Inc, 1130 Sherbrooke Street West, Montreal, Quebec, Canada, H3A 2M8
Email: jtmckeev@ghgsat.com

Frederic Piedboeuf
GHGSat Inc, 1130 Sherbrooke Street West, Montreal, Quebec, Canada, H3A 2M8
Email: fpiedboeuf@ghgsat.com

Antoine Ramier
GHGSat Inc, 1130 Sherbrooke Street West, Montreal, Quebec, Canada, H3A 2M8
Email: aramier@ghgsat.com
orcid.org/0000-0003-0728-1725

Mathias Strupler
GHGSat Inc, 1130 Sherbrooke Street West, Montreal, Quebec, Canada, H3A 2M8
Email: mas@ghgsat.com
orcid.org/0000-0002-9265-4604

NOTES

The authors declare no competing financial interest.

AUTHOR CONTRIBUTIONS

DJ conceived the study, developed the estimation model, performed the analysis, and wrote the manuscript; AA helped develop the estimation model; SAB, ADR, VF, JH, and KM developed the facility emission time series dataset; JM, FP, AR, and MS helped produce the underlying GHGSat plume and retrieval data; All authors contributed to the interpretation of the results and editing of the manuscript.

ACKNOWLEDGEMENTS

We acknowledge work from Jake Wilson, Josh Sampson and Marianne Girard for help creating the facility-attributed dataset.

REFERENCES

(1) Intergovernmental Panel on Climate Change (IPCC). *Climate Change 2021 – The Physical Science Basis*; Cambridge University Press, 2023. https://doi.org/10.1017/9781009157896.

(2) Saunois, M.; Martinez, A.; Poulter, B.; Zhang, Z.; Raymond, P. A.; Regnier, P.; Canadell, J. G.; Jackson, R. B.; Patra, P. K.; Bousquet, P.; Ciais, P.; Dlugokencky, E. J.; Lan, X.; Allen, G. H.; Bastviken, D.; Beerling, D. J.; Belikov, D. A.; Blake, D. R.; Castaldi, S.; Crippa, M.; Deemer, B. R.; Dennison, F.; Etiope, G.; Gedney, N.; Höglund-Isaksson, L.; Holgerson, M. A.; Hopcroft, P. O.; Hugelius, G.; Ito, A.; Jain, A. K.; Janardanan, R.; Johnson, M. S.; Kleinen, T.; Krummel, P. B.; Lauerwald, R.; Li, T.; Liu, X.; McDonald, K. C.; Melton, J. R.; Mühle, J.; Müller, J.; Murguia-Flores, F.; Niwa, Y.; Noce, S.; Pan, S.; Parker, R. J.; Peng, C.; Ramonet, M.; Riley, W. J.; Rocher-Ros, G.; Rosentreter, J. A.; Sasakawa, M.; Segers, A.; Smith, S. J.; Stanley, E. H.; Thanwerdas, J.; Tian, H.; Tsuruta, A.; Tubiello, F. N.; Weber, T. S.; van der Werf, G. R.; Worthy, D. E. J.; Xi, Y.; Yoshida, Y.; Zhang, W.; Zheng, B.; Zhu, Q.; Zhu, Q.; Zhuang, Q. Global Methane Budget 2000–2020. *Earth Syst. Sci. Data* **2025**, *17* (5), 1873–1958. https://doi.org/10.5194/essd-17-1873-2025.

(3) U.S. Environmental Protection Agency. *Methane Super Emitter Program*. https://www.epa.gov/compliance/methane-super-emitter-program (accessed 2026-08-17).

(4) United Nations Environment Programme. *Methane Alert and Response System (MARS)*. https://www.unep.org/topics/energy/methane/methane-alert-and-response-system-mars (accessed 2026-08-17).

(5) United Nations Environment Programme. *Oil and Gas Methane Partnership (OGMP) 2.0 Reporting Framework*. United Nations Environment Programme. https://www.ogmpartnership.org/ (accessed 2026-08-17).

(6) Johnson, M. R.; Conrad, B. M.; Tyner, D. R. Creating Measurement-Based Oil and Gas Sector Methane Inventories Using Source-Resolved Aerial Surveys. *Commun. Earth Environ.* **2023**, *4* (1). https://doi.org/10.1038/s43247-023-00769-7.

(7) Sherwin, E. D.; Rutherford, J. S.; Zhang, Z.; Chen, Y.; Wetherley, E. B.; Yakovlev, P. V.; Berman, E. S. F.; Jones, B. B.; Cusworth, D. H.; Thorpe, A. K.; Ayasse, A. K.; Duren, R. M.; Brandt, A. R. US Oil and Gas System Emissions from Nearly One Million Aerial Site Measurements. *Nature* **2024**, *627* (8003), 328–334. https://doi.org/10.1038/s41586-024-07117-5.

(8) Donahue, C. P.; Oberoi, K.; Dillon, J. W.; Hengst, V.; Kennedy, B.; Kearney, W.; Lennox, J.; Rehbein, E.; Sykes, R.; Dudiak, C. D.; Altamura, D. T.; Doherty, G.; Roos, P. A.; Brasseur, J. K.; Thorpe, M. J. Aerial LiDAR-Based, Source-Resolved Methane Emissions Inventory: Permian Basin Case Study for Benchmarking U.S. Emissions. *Environ. Sci. Technol.* **2026**, *60* (19), 13968–13979. https://doi.org/10.1021/acs.est.5c15184.

(9) Jervis, D.; Girard, M.; MacLean, J.-P. W.; Marshall, D.; McKeever, J.; Strupler, M.; Ramier, A.; Tarrant, E.; Young, D.; Maasakkers, J. D.; Aben, I.; Scarpelli, T. R. Global

Energy Sector Methane Emissions Estimated by Using Facility-Level Satellite Observations. *Science (1979)*. **2025**, *390* (6778), 1151–1155. https://doi.org/10.1126/science.adv3183.

(10) Adekomi, A. A.; Yang, S. L.; Stokes, S.; Ravikumar, A. P. Cause-Informed Framework for Risk-Targeted Methane Emission Mitigation in Oil and Gas Operations. *Nat. Commun.* **2026**. https://doi.org/10.1038/s41467-026-72607-1.

(11) Cusworth, D. H.; Duren, R. M.; Thorpe, A. K.; Pandey, S.; Maasakkers, J. D.; Aben, I.; Jervis, D.; Varon, D. J.; Jacob, D. J.; Randles, C. A.; others. Multisatellite Imaging of a Gas Well Blowout Enables Quantification of Total Methane Emissions. *Geophys. Res. Lett.* **2021**, *48* (2), e2020GL090864.

(12) Harris, S. J.; Schwietzke, S.; France, J. L.; Velandia Salinas, N.; Meixus Fernandez, T.; Randles, C.; Guanter, L.; Irakulis-Loitxate, I.; Calcan, A.; Aben, I.; Abrahamsson, K.; Balcombe, P.; Berchet, A.; Biddle, L. C.; Bittig, H. C.; Böttcher, C.; Bouvard, T.; Broström, G.; Bruch, V.; Cassiani, M.; Chipperfield, M. P.; Ciais, P.; Damm, E.; Dammers, E.; Denier van der Gon, H.; Dogniaux, M.; Dowd, E.; Dupouy, F.; Eckhardt, S.; Evangeliou, N.; Feng, W.; Jia, M.; Jiang, F.; Kaiser-Weiss, A. K.; Kamoun, I.; Kerridge, B. J.; Lampert, A.; Lana, J.; Li, F.; Maasakkers, J. D.; Maclean, J. P. W.; Mamtimin, B.; Marshall, J.; Mauger, G.; Mekkas, A.; Mielke, C.; Mohrmann, M.; Moore, D. P.; Nanni, R.; Pätzold, F.; Pison, I.; Pisso, I.; Platt, S. M.; Préa, R.; Queste, B. Y.; Ramonet, M.; Rehder, G.; Remedios, J. J.; Reum, F.; Roiger, A.; Schmidbauer, N.; Siddans, R.; Sunkisala, A.; Thompson, R. L.; Varon, D. J.; Ventress, L. J.; Wilson, C.; Zhang, Y. Methane Emissions from the Nord Stream Subsea Pipeline Leaks. *Nature* **2025**, *637* (8048), 1124–1130. https://doi.org/10.1038/s41586-024-08396-8.

(13) Guanter, L.; Roger, J.; Sharma, S.; Valverde, A.; Irakulis-Loitxate, I.; Gorroño, J.; Zhang, X.; Schuit, B. J.; Maasakkers, J. D.; Aben, I.; Groshenry, A.; Benoit, A.; Peyle, Q.; Zavala-Araiza, D. Multisatellite Data Depicts a Record-Breaking Methane Leak from a Well Blowout. *Environ. Sci. Technol. Lett.* **2024**, *11* (8), 825–830. https://doi.org/10.1021/acs.estlett.4c00399.

(14) Ayasse, A. K.; Cusworth, D. H.; Howell, K.; O'Neill, K.; Conrad, B. M.; Johnson, M. R.; Heckler, J.; Asner, G. P.; Duren, R. Probability of Detection and Multi-Sensor Persistence of Methane Emissions from Coincident Airborne and Satellite Observations. *Environ. Sci. Technol.* **2024**. https://doi.org/10.1021/acs.est.4c06702.

(15) Guanter, L.; Roger, J.; Warren, J.; Sargent, M.; Zhang, Z.; Roche, S.; Miller, C. C.; Steiner, M.; Hadfield, H.; Omara, M.; Williams, J.; MacKay, K.; Franklin, J. E.; Luo, B.; Wofsy, S. C.; Hamburg, S. P.; Gautam, R. Surveying Methane Point-Source Super-Emissions across Oil and Gas Basins with MethaneSAT. *Atmos. Chem. Phys.* **2026**, *26* (4), 2941–2963. https://doi.org/10.5194/acp-26-2941-2026.

(16) Williams, J. P.; Benmergui, J.; Knapp, M.; Omara, M.; Himmelberger, A.; Kyzivat, E.; Weatherby, K.; Lyke, B.; Warren, J.; MacKay, K.; Ayvazov, S.; Russi, M.; LoFaso, N.; Melendez, T.; Miller, C. C.; Roche, S.; Sargent, M.; Franklin, J.; Nasr, M.; Zhang, Z.; Miller, D. J.; Luo, B.; Guanter, L.; Hamburg, S. P.; Wofsy, S. C.; Gautam, R. Methane

Intensity and Emissions across Major Oil and Gas Basins and Individual Jurisdictions Using MethaneSAT Observations. *Atmos. Chem. Phys.* **2026**, *26* (9), 5961–5981. https://doi.org/10.5194/acp-26-5961-2026.

(17) Jervis, D.; MacLean, J. P. W.; McKeever, J.; Ramier, A.; Strupler, M. Joint Estimation of the Global Facility-Scale Oil-Gas Methane Emission Rate Distribution and Survey-Mode Detection Probabilities from Multiple Satellite Systems. *Environ. Sci. Technol.* **2026**, *60* (21), 14961–14970. https://doi.org/10.1021/acs.est.5c17089.

(18) Gelman, A.; Carlin, J. B.; Stern, H. S.; Dunson, D. B.; Vehtari, A.; Rubin, D. B.; Carlin, J.; Stern, H.; Rubin, D.; Dunson, D. *Bayesian Data Analysis (3rd Edition)*; 2013. https://doi.org/10.1201/b16018.

(19) Chen, Y.; Sherwin, E. D.; Berman, E. S. F.; Jones, B. B.; Gordon, M. P.; Wetherley, E. B.; Kort, E. A.; Brandt, A. R. Quantifying Regional Methane Emissions in the New Mexico Permian Basin with a Comprehensive Aerial Survey. *Environ. Sci. Technol.* **2022**, *56* (7), 4317–4323. https://doi.org/10.1021/acs.est.1c06458.

(20) Ehret, T.; De Truchis, A.; Mazzolini, M.; Morel, J. M.; D'Aspremont, A.; Lauvaux, T.; Duren, R.; Cusworth, D.; Facciolo, G. Global Tracking and Quantification of Oil and Gas Methane Emissions from Recurrent Sentinel-2 Imagery. *Environ. Sci. Technol.* **2022**, *56* (14), 10517–10529. https://doi.org/10.1021/acs.est.1c08575.

(21) Lauvaux, T.; Giron, C.; Mazzolini, M.; d'Aspremont, A.; Duren, R.; Cusworth, D.; Shindell, D.; Ciais, P. Global Assessment of Oil and Gas Methane Ultra-Emitters. *Science (1979).* **2022**, *375* (6580), 557–561. https://doi.org/10.1126/science.abj4351.

(22) Varon, D. J.; Jacob, D. J.; Estrada, L. A.; Balasus, N.; East, J. D.; Pendergrass, D. C.; Chen, Z.; Sulprizio, M.; Omara, M.; Gautam, R.; Barkley, Z. R.; Saldaña, F. J. C.; Reidy, E. K.; Kamdar, H.; Sherwin, E. D.; Biraud, S. C.; Jervis, D.; Pandey, S.; Worden, J. R.; Bowman, K. W.; Maasakkers, J. D.; Kleinberg, R. L. Seasonality and Declining Intensity of Methane Emissions from the Permian and Nearby US Oil and Gas Basins. *Environ. Sci. Technol.* **2026**, *60* (1), 425–435. https://doi.org/10.1021/acs.est.5c08745.

(23) Varon, D. J.; Jacob, D. J.; Hmiel, B.; Gautam, R.; Lyon, D. R.; Omara, M.; Sulprizio, M.; Shen, L.; Pendergrass, D.; Nesser, H.; Qu, Z.; Barkley, Z. R.; Miles, N. L.; Richardson, S. J.; Davis, K. J.; Pandey, S.; Lu, X.; Lorente, A.; Borsdorff, T.; Maasakkers, J. D.; Aben, I. Continuous Weekly Monitoring of Methane Emissions from the Permian Basin by Inversion of TROPOMI Satellite Observations. *Atmos. Chem. Phys.* **2023**, *23* (13), 7503–7520. https://doi.org/10.5194/acp-23-7503-2023.

(24) Sherwin, E. D.; Rutherford, J. S.; Chen, Y.; Aminfard, S.; Kort, E. A.; Jackson, R. B.; Brandt, A. R. Single-Blind Validation of Space-Based Point-Source Detection and Quantification of Onshore Methane Emissions. *Sci. Rep.* **2023**, *13* (1). https://doi.org/10.1038/s41598-023-30761-2.

(25) Ramier, A.; Girard, M.; Jervis, D.; Maclean, J.-P.; Marshall, D.; Mckeever, J.; Strupler, M.; Tarrant, E.; Young, D. *High-Resolution Methane Detection with the GHGSat Constellation*; IAF. https://doi.org/10.31223/X5FF0X.

(26) Conrad, B. M.; Tyner, D. R.; Johnson, M. R. Robust Probabilities of Detection and Quantification Uncertainty for Aerial Methane Detection: Examples for Three Airborne Technologies. *Remote Sens. Environ.* **2023**, *288*, 113499. https://doi.org/10.1016/j.rse.2023.113499.

(27) Shen, L.; Gautam, R.; Omara, M.; Zavala-Araiza, D.; Maasakkers, J. D.; Scarpelli, T. R.; Lorente, A.; Lyon, D.; Sheng, J.; Varon, D. J.; Nesser, H.; Qu, Z.; Lu, X.; Sulprizio, M. P.; Hamburg, S. P.; Jacob, D. J. Satellite Quantification of Oil and Natural Gas Methane Emissions in the US and Canada Including Contributions from Individual Basins. *Atmos. Chem. Phys.* **2022**, *22* (17), 11203–11215. https://doi.org/10.5194/acp-22-11203-2022.

(28) Cusworth, D. H.; Duren, R. M.; Thorpe, A. K.; Olson-Duvall, W.; Heckler, J.; Chapman, J. W.; Eastwood, M. L.; Helmlinger, M. C.; Green, R. O.; Asner, G. P.; Dennison, P. E.; Miller, C. E. Intermittency of Large Methane Emitters in the Permian Basin. *Environ. Sci. Technol. Lett.* **2021**, *8* (7), 567–573. https://doi.org/10.1021/acs.estlett.1c00173.

(29) Pandey, S.; Worden, J.; Cusworth, D. H.; Varon, D. J.; Thill, M. D.; Jacob, D. J.; Bowman, K. W. Relating Multi-Scale Plume Detection and Area Estimates of Methane Emissions: A Theoretical and Empirical Analysis. *Environ. Sci. Technol.* **2025**, *59* (16), 7931–7947. https://doi.org/10.1021/acs.est.4c07415.

(30) Wilson, J.; Foing, V.; Andersson-Bastable, S.; Delgado-Recke, A.; Hayden, J.; Jervis, D. *Plume Origin Localisation with Computer Vision*. https://doi.org/10.31223/X5RR4B.

(31) Omara, M.; Gautam, R.; O'Brien, M. A.; Himmelberger, A.; Franco, A.; Meisenhelder, K.; Hauser, G.; Lyon, D. R.; Chulakadabba, A.; Miller, C. C.; Franklin, J.; Wofsy, S. C.; Hamburg, S. P. Developing a Spatially Explicit Global Oil and Gas Infrastructure Database for Characterizing Methane Emission Sources at High Resolution. *Earth Syst. Sci. Data* **2023**, *15* (8), 3761–3790. https://doi.org/10.5194/essd-15-3761-2023.

(32) Mckeever, J.; Jervis, D. *Validation and Metrics for Emissions Detection by Satellite*; 2022. https://www.ghgsat.com/en/case-studies/validation-and-metrics-for-emissions-detection-by-satellite/ (accessed 2024-04-25).

(33) Jervis, D.; Maclean, J.-P. W.; Mckeever, J.; Strupler, M.; Ramier, A. *Estimating the Global Oil-Gas Methane Emission Rate Distribution at Facility Scale Using Multiple Satellite Systems*. https://methanedata.unep.org/.

(34) Jacob, D. J.; Turner, A. J.; Maasakkers, J. D.; Sheng, J.; Sun, K.; Liu, X.; Chance, K.; Aben, I.; McKeever, J.; Frankenberg, C. Satellite Observations of Atmospheric Methane and Their Value for Quantifying Methane Emissions. *Atmos. Chem. Phys.* **2016**, *16* (22), 14371–14396.

(35) Bruno, J. H.; Jervis, D.; Varon, D. J.; Jacob, D. J. U-Plume: Automated Algorithm for Plume Detection and Source Quantification by Satellite Point-Source Imagers. *Atmos. Meas. Tech.* **2024**, *17* (9), 2625–2636. https://doi.org/10.5194/amt-17-2625-2024.

(36) Varon, D. J.; Jacob, D. J.; McKeever, J.; Jervis, D.; Durak, B. O. A.; Xia, Y.; Huang, Y. Quantifying Methane Point Sources from Fine-Scale Satellite Observations of Atmospheric Methane Plumes. *Atmos. Meas. Tech.* **2018**, *11* (10), 5673–5686.

	Mean observations per facility [95% range]	Mean annual large-emitter emission rate [95% range] (kg h^{-1})	Large emitter persistence [95% range]
2023 Wells	4.1 [1, 17]	*0.46 [0.40, 0.53]*	*0.0012 [0.0010, 0.0015]*
2024 Wells	5.0 [1, 18]	*0.46 [0.40, 0.53]*	*0.0012 [0.0010, 0.0015]*
2025 Wells	6.4 [1, 19]	*0.46 [0.40, 0.53]*	*0.0012 [0.0010, 0.0015]*
2023 Compressor/Gathering	5.0 [1, 20]	35.9 [16.7, 87.1]	0.0912 [0.0608, 0.1813]
2024 Compressor/Gathering	7.2 [1, 20]	34.0 [14.9, 97.4]	0.0908 [0.0618, 0.1885]
2025 Compressor/Gathering	8.5 [1, 21]	32.2 [15.0, 93.2]	0.0894 [0.0638, 0.1786]
2023 Gas processing plant	4.3 [1, 14]	139.7 [75.8, 330.8]	0.2493 [0.1420, 0.5029]
2024 Gas processing plant	4.9 [1, 18]	144.3 [55.3, 412.5]	0.2490 [0.1269, 0.5355]
2025 Gas processing plant	6.9 [1, 18]	144.2 [52.0, 389.8]	0.2380 [0.1097, 0.5515]

Table 1: Summary table of 2023-2025 Permian Basin observations, annual large emissions, and large-emitter persistence estimates. Numbers in italics are derived from prior means and bootstrap estimates.

	Observed facilities	Total facilities	Observed total (Mt y^{-1})	Scaled total (Mt y^{-1})
2023 Wells	76117	173840	*0.3095 [0.2670, 0.3526]*	*0.7069 [0.6098, 0.8053]*
2023 Compressor/Gathering	1320	2417	0.4156 [0.3839, 0.4647]	0.7609 [0.7029, 0.8509]
2023 Gas processing plant	112	189	0.1370 [0.1258, 0.1492]	0.2312 [0.2123, 0.2518]
2023 All classes total	**77549**	**176446**	**0.8621 [0.8069, 0.9258]**	**1.6990 [1.5813, 1.8301]**
2024 Wells	101408	173840	*0.4124 [0.3557, 0.4697]*	*0.7069 [0.6098, 0.8053]*
2024 Compressor/Gathering	1556	2417	0.4629 [0.4366, 0.4938]	0.7190 [0.6783, 0.7671]
2024 Gas processing plant	130	189	0.1643 [0.1485, 0.1831]	0.2388 [0.2159, 0.2663]
2024 All classes total	**103094**	**176446**	**1.0395 [0.9739, 1.1054]**	**1.6647 [1.5575, 1.7747]**
2025 Wells	93721	173840	*0.3811 [0.3287, 0.4341]*	*0.7069 [0.6098, 0.8053]*
2025 Compressor/Gathering	1584	2417	0.4470 [0.4259, 0.4709]	0.6820 [0.6499, 0.7185]
2025 Gas processing plant	132	189	0.1667 [0.1464, 0.1917]	0.2387 [0.2097, 0.2744]
2025 All classes total	**95437**	**176446**	**0.9948 [0.9366, 1.0571]**	**1.6276 [1.5247, 1.7384]**

Table 2: Total 2023-2025 Permian Basin large-emitter annual emission estimates. Numbers in italics are derived exclusively from prior means and bootstrap estimates.

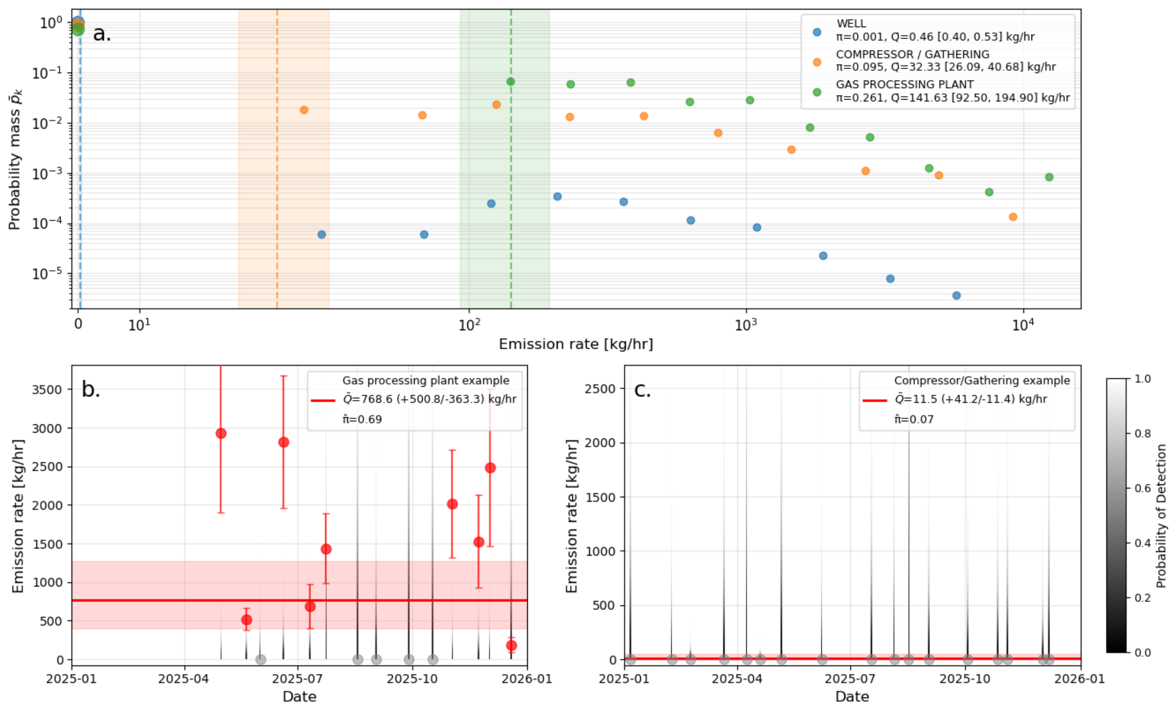

Figure 2: Prior emission-rate distributions and example facility time-series emission data and estimates: (a) The prior emission-rate distribution $\bar{p}_k$ for the three different facility classes: wells, compressor/gathering, and gas processing plants. The facility class average emission rate (annotated and illustrated with dashed vertical line on the plot), and the facility class average large-emitter persistence (annotated) are noted for each; (b) an example gas processing plant emission time series (red markers with error bars are detected and quantified emission rates, gray markers are observations without plume detections, vertical shaded bars visualize the per-observation probability of detection) with mean annual large-emitter emission rate ($\bar{Q}$ is horizontal red line, shaded region is the 95% credibility interval) and large emissions persistence $\bar{\pi}$ (annotated in legend); (c) an example compressor/gathering facility where all observations resulted in non-detections, though we still estimate a non-zero annual emission rate (with the lower bound of the 95% credibility interval reaching close to zero kg h^{-1}).

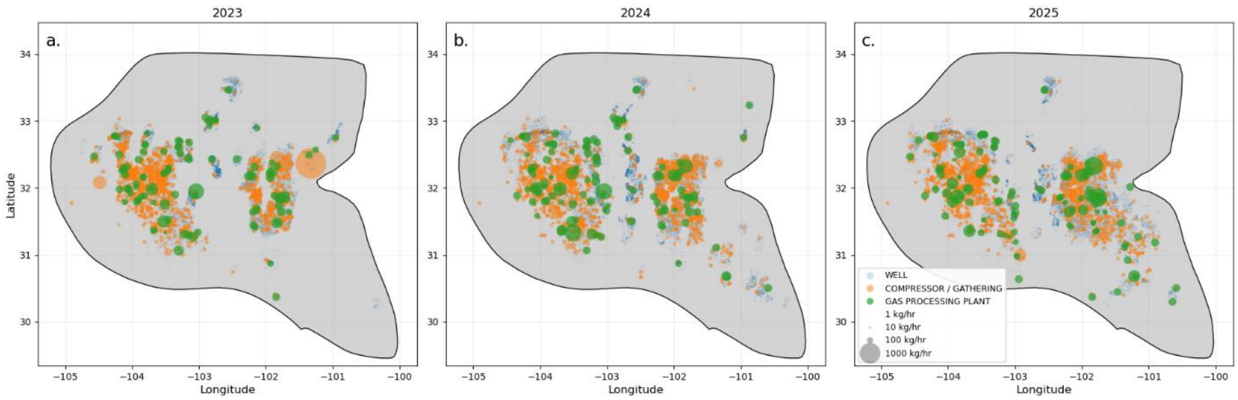

Figure 2: Map of facility annual emissions estimates in the Permian Basin in 2023, 2024, and 2025. The marker area is proportional to the magnitude of the annual emission estimate.

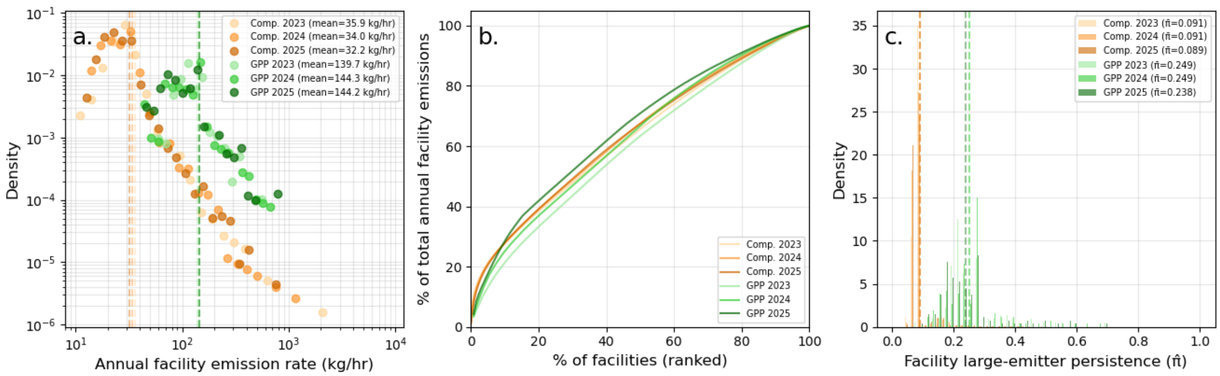

Figure 3: Distribution of midstream facility annual emission and persistence estimates. a) Distribution of annual facility emission estimates from compressor/gathering stations and gas processing plants; b) Cumulative distribution of total annual facility emission estimates versus the cumulative number of facilities; c) Distribution of facility large-emitter persistence from compressor/gathering stations and gas processing plants.

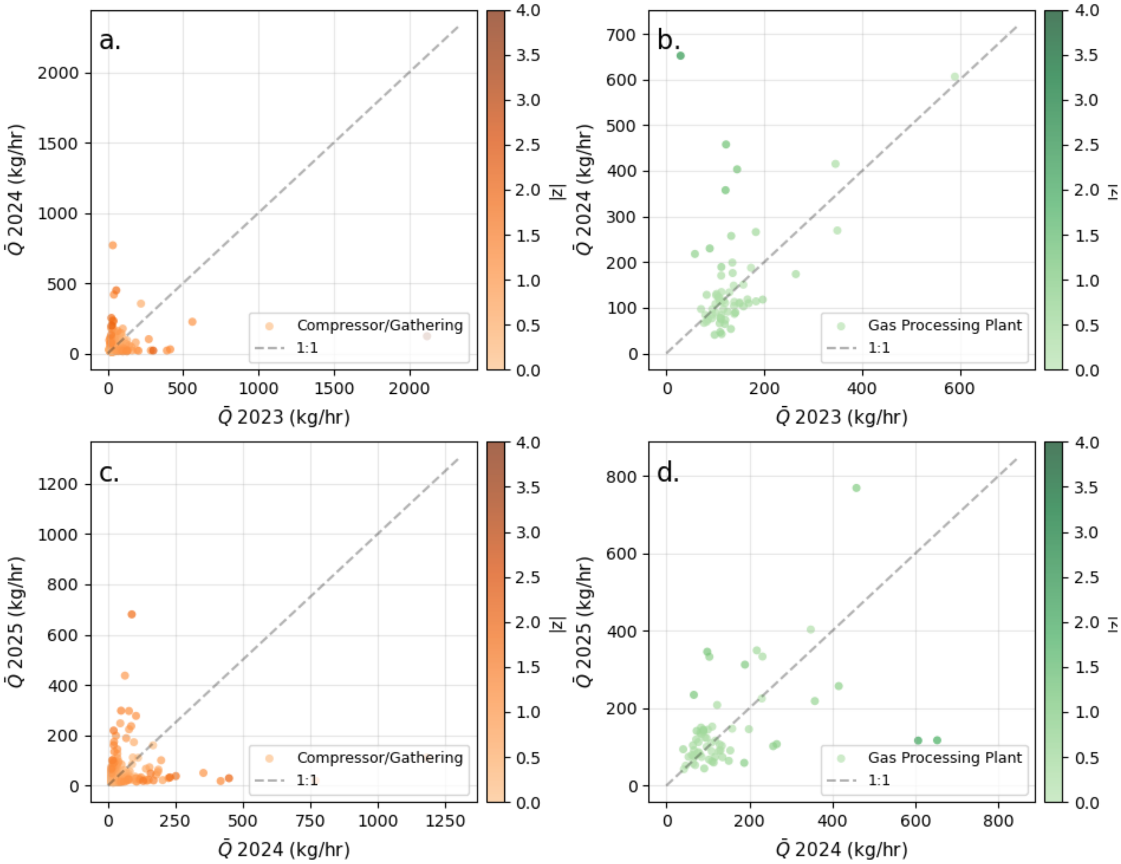

Figure 4: Interannual variability in midstream facility annual emission rates. Each parity plot shows a comparison between matched facilities of the same class in subsequent years, with markers coloured by the z-score: a) compressor/gathering stations between 2023-2024; b) gas plants between 2023-2024; c) compressor/gathering stations between 2024-2025; d) gas plants between 2024-2025.

SUPPORTING INFORMATION: Recurrent High-Resolution Satellite Observations Quantify Facility-Resolved Annual Large-Emitter Methane Emissions in the Permian Basin

Dylan Jervis[1], Alessandro Ambler[1], Simon Andersson-Bastable[1], Amanda Delgado-Recke[1], Victoria Foing[1], Jack Hayden[1], Krishna Mooroogen[1], Jason McKeever[1], Frederic Piedboeuf[1], Antoine Ramier[1], and Mathias Strupler[1]*

[1]GHGSat Inc, 1130 Sherbrooke Street West, Montreal, QC, Canada, H3A 2M8

*Email: dylan.jervis@ghgsat.com

Summary: 15 pages, 2 figures

TABLE OF CONTENTS

S1 Plume origin estimation

The origin of each detected methane plume was estimated using a computer-vision model described in Ref[30]. The model uses three spatially co-registered inputs derived for each observation: the methane signal-to-error-ratio field, a binary mask delineating the detected plume, and a graphical representation of wind direction and speed. A U-Net model produces a pixel-level spatial probability distribution for the plume origin rather than a single deterministic source location, thereby representing uncertainty arising from diffuse plume structure and wind-field uncertainty. The model was trained using expert-annotated origins for 6,667 oil and gas plumes and validated on an independent set of 3,333 plumes. The expected location of the predicted probability distribution had a median separation of 64.2 m from the expert-annotated origin, with 65.1% of predicted origins falling within 100 m. Full details of the model architecture, training data, probability calibration, and validation are provided in Ref[30].

S2 Facility Detector

Facility-level plume attribution requires spatial representations of the locations and extents of candidate oil and gas facilities. Point-based infrastructure databases may contain positional errors, represent administrative rather than physical locations, or fail to capture the spatial extent of a constructed pad. We therefore represented each facility as a polygon footprint derived from visible satellite imagery. A facility footprint was defined as the constructed pad containing a collection of related oil and gas equipment, such as a well pad, compressor station, or gas processing plant. These polygons provided the spatial information used to associate plume-origin probability distributions with candidate facilities.

Facility footprints were detected from the 10 m red, green, and blue bands of Sentinel-2 Level-2A imagery using an instance-segmentation model. The model used the Mask R-CNN architecture with a ResNet-50 feature-pyramid-network backbone, implemented in Detectron2 and initialized from a model pretrained on the Cityscapes dataset. The training dataset comprised 2,767 Sentinel-2 image tiles, each containing 128 × 128 pixels, and 16,682 polygon annotations derived from co-located OpenStreetMap features. Candidate OpenStreetMap records were selected using oil- and gas-related labels, including oil, natural_gas, gas, oil_treating_facility, natural_gas_compressor_station, well_cluster, and wellsite. The resulting dataset was manually screened to remove urban and other visibly non-oil-and-gas features. Most training polygons were relatively small: 79.3% had areas below 1 ha, 20.6% had areas of 1–25 ha, and 0.1% exceeded 25 ha.

Inference was conducted independently using Sentinel-2 imagery from 2018–2024. The Permian Basin was divided into overlapping spatial tiles, predictions intersecting tile boundaries were merged, and annual detections were combined additively to increase recall. The multi-year procedure identified 454,813 candidate footprint polygons; a metadata-based filtering procedure, using independent facility locations, road connectivity, and model confidence, flagged approximately 10% as potential false positives. Multi-year inference produced a holdout-set recall approaching 0.6 at an intersection-over-union threshold of 0.5, exceeding that obtained from any single inference year. Because the relatively coarse Sentinel-2 resolution can confuse constructed pads with bright roads or natural surfaces, footprints near attributed methane plumes were additionally reviewed and corrected through a human-in-the-loop quality-control step.

Finally, detected polygons were spatially intersected with external oil and gas infrastructure databases, including Enverus and the Oil and Gas Infrastructure Mapping database[31], to attach facility metadata such as facility identity, operator, operating status, and reported infrastructure type. Source database labels were incorporated into the facility classes used in this analysis: well sites, compressor and gathering stations, and gas processing plants. Where multiple records or categories intersected a polygon, gas processing plant classifications were given precedence, followed by well-site classifications and then compressor or gathering classifications. Polygons without sufficiently reliable class information were retained as unclassified and excluded from class-specific analyses.

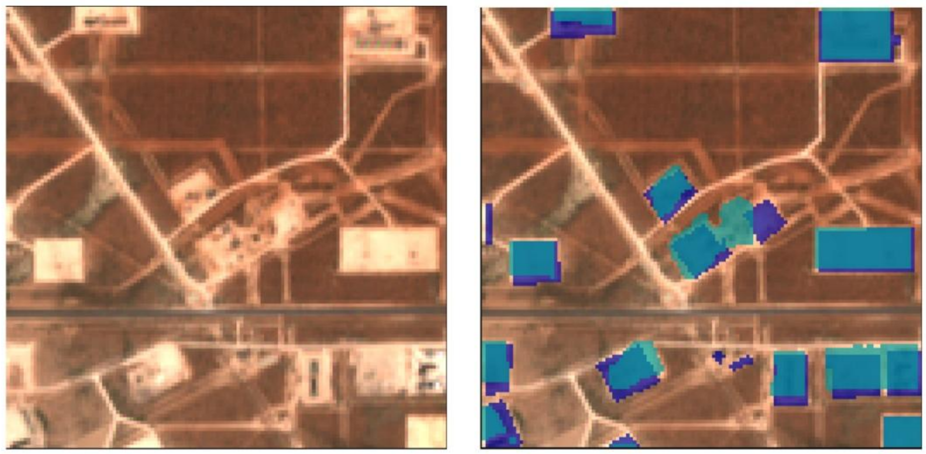

Figure S3 Example holdout test image. Left): Sentinel-2 RGB imagery. Right): Sentinel-2 RGB imagery with annotations (dark blue) and predicted polygons (teal) overlayed. Some predictions correctly identify single blocks for footprints as seen in the basemap, yet truth annotations are labeled as separate detections due to using high-res data to construct them.

S3 Plume-Facility Attribution Model

Plume detections were attributed to candidate facility footprints using a probabilistic method. Let $p(x, y)$ denote the normalized spatial probability density of the plume origin and let $f_i(x, y)$ be the binary footprint mask for candidate facility i, equal to one inside the mapped facility boundary and zero elsewhere. For each candidate facility, we calculated an area-normalized overlap score,

$$S_i = \frac{\int p(x,y) f_i(x,y) dx\, dy}{\int f_i(x,y) dx\, dy} \qquad (S1)$$

Where the integration was over the high-probability plume-origin region R used for attribution. The facility attribution probability was obtained by normalizing the scores across all candidate facilities,

$$P_\mathrm{i} = \frac{S_\mathrm{i}}{\sum S_\mathrm{j}} \qquad (S2)$$

The area normalization prevents larger facility footprints from receiving greater attribution probability solely because they cover more pixels. The integration region R was defined as the smallest region containing the most probable 80% of the plume-origin probability mass, thereby scaling the attribution domain to the spatial uncertainty of each plume-origin estimate. This avoids averaging over large areas with negligible plume-origin probability, which can otherwise bias area-normalized overlap scores when the predicted origin region is small relative to the facility footprints. Facilities that did not intersect R were assigned zero attribution probability. Each plume was attributed to the facility with the largest resulting attribution probability, with the following conditions: the plume origin function had to be sufficiently peaked, $\max(p(x, y)) > 0.2$, to discriminate against overly uncertain plume origin estimation (indicating, for example, from dis-attached or orphaned plumes); there had to be sufficient overlap between the plume and all facilities in the observation, $\sum_i P_i > 0.05$; there had to be a sufficient difference in attribution probability between the most likely P_I and second most likely P_{II} facility, $\frac{P_I}{P_{II}} > 1.5$. Plumes that did not meet these criteria were excluded from the analysis.

S4 Per-observation POD

The probability of detection (POD) for a methane point-source imager such as GHGSat is the probability that an emission with rate Qwill be detected. Importantly, the POD depends on both observational conditions (i.e. the wind speed u that a plume is emitted into, the methane column density error $\delta\Omega_{CH_4}$ in the local area, and the spatial resolution gsd), as well as the inspection conditions, i.e., the effective scrutiny applied when assessing whether a plume is present at a given location.

GHGSat's POD has been estimated using two main approaches: (i) controlled-release measurement campaigns, including internal studies [25,32] and a single-blind, independently organized study [24]; and (ii) inference from emission-rate distributions [33]. Each approach has limitations. Controlled-release analyses typically parameterize POD primarily as a function of Q (and sometimes u), but do not explicitly capture dependence on $\delta\Omega_{\mathrm{CH_4}}$, and they reflect enhanced inspection attention because the source location is known a priori. Conversely, the emission-rate distribution approach uses large volumes of operational detections (e.g., a full year in the oil-and-gas sector) to estimate POD under average observational and inspection conditions, but does not resolve how the POD varies with u, $\delta\Omega_{\mathrm{CH_4}}$, or GSD.

Here, we estimate the following per-observation POD function:

$$POD(Q;\boldsymbol{\theta_o};\boldsymbol{\theta_I}) = \frac{1}{2}\left(1 + \mathrm{erf}\left(\frac{\log\big(z(Q;\boldsymbol{\theta_o})\big) - \mu_I}{\sigma_I}\right)\right) \tag{S3}$$

where $\boldsymbol{\theta_o} = (gsd, u, \delta\Omega_{CH_4})$ is the observation condition parameter vector, $\boldsymbol{\theta_I} = (\mu_I, \sigma_I)$ is the inspection condition parameter vector, and the dimension-less plume signal-to-noise function $z(Q;\boldsymbol{\theta_o})$ is given by:

$$z(Q;\boldsymbol{\theta_o}) = \frac{Q}{gsd \cdot u \cdot \delta\Omega_{CH_4}} \tag{$S4$}$$

with all quantities expressed in SI units. If the more commonly used units Q [kg h^{-1}], gsd [m], u [m s^{-1}], and $\delta\Omega_{CH_4}$ [mol m^{-2}], this becomes

$$z(Q;\boldsymbol{\theta_o}) = \frac{Q}{3.6 \cdot M_{CH_4} \cdot gsd \cdot u \cdot \delta\Omega_{CH_4}} \tag{$S5$}$$

Where M_{CH_4}=16.04 g mol^{-1} is the molar mass of methane. This form follows directly from dimensional and physical considerations. It was originally introduced in Ref [34], but has also appeared with some variation in Refs [26,35]. For some representative values of $(\boldsymbol{\theta_o}, \boldsymbol{\theta_I})$, Equation (1) produces a smooth function with low detection probability at small Q and near-certain detection at large Q, as expected.

The observation condition parameter vector $\boldsymbol{\theta_o} = (gsd, u, \delta\Omega_{CH_4})$ comprises the spatial resolution gsd, wind speed u, and methane column density error $\delta\Omega_{CH_4}$. For the gsd, we assume a constant ground sampling distance of gsd=30 m. While GSD varies modestly with viewing geometry and target altitude, these effects are typically small (<10%) for the observations considered here.

Wind speed u is sampled at the center of each observation (target latitude/longitude). The methane column density error is defined as

$$\delta\Omega_{CH_4} = \left\langle \Delta\Omega_{CH_4} \right\rangle_{\sigma_k} |_{(\psi,\phi)} \tag{S6}$$

where $\Delta\Omega_{CH_4}$ is the per-pixel posterior uncertainty estimated from the methane column density retrieval. The operator $\langle \dots \rangle_{\sigma_k}$ represents two-dimensional Gaussian filtering with kernel width σ_k= 5 pixels, and the filtered error field is evaluated at the lat/lon location of interest (ψ, ϕ) (e.g. a facility location). We apply this spatial filtering to reflect the fact that methane plumes are spatially correlated enhancements. Consequently, the error relevant for detecting a small plume is the correlated retrieval uncertainty at low emission rate plume length scales, rather than pixel-scale noise.

We estimate the inspection condition parameter vector $\boldsymbol{\theta_I} = (\mu_I, \sigma_I)$ by fitting the measured emissions rates to an underlying emission rate distribution, similar to what was done in Ref [33]. Let $\boldsymbol{Q} = \{Q_1, Q_2, \dots, Q_N\}$ be the detected emission rates. The probability density distribution of a detected emission Q_i is

$$f(Q_i|\boldsymbol{\theta_o};\boldsymbol{\theta_I}) = \frac{POD(Q_i;\boldsymbol{\theta_o};\boldsymbol{\theta_I})\rho(Q_i)}{Z} \tag{S7}$$

and, correspondingly, the likelihood of detecting the emission rates $\boldsymbol{Q}$ is given by the product of these terms

$$\mathcal{L}(\boldsymbol{\theta_I}|\,\boldsymbol{Q}) = \prod_{i=1}^{N} f(Q_i|\boldsymbol{\theta_o};\boldsymbol{\theta_I})\,. \tag{S8}$$

Here, the underlying true emission rate density distribution is modelled as a lognormal

$$\rho(Q) = \frac{1}{Q\sigma_k\sqrt{2\pi}} e^{-\frac{(\ln(Q)-\mu_{PDF})^2}{2\sigma_{PDF}^2}} \tag{S9}$$

With parameters $(\mu_{PDF}, \sigma_{PDF}) = (-6.72 + \log(1000)\,, 2.56)$ fixed at the values found in [33](for emission rates expressed in units of kg h^{-1}); and the normalization constant $Z = \int_0^{\infty} \overline{POD}(Q)\rho(Q)dQ$is defined using the average POD over all detections $\overline{POD}(Q) = \frac{1}{N}\sum POD\big(Q_i; \boldsymbol{\theta_{o;i}}; \boldsymbol{\theta_I}\big)$.

After maximizing the likelihood, we estimate the inspection condition parameters over all O&G sector detections in 2024 to be $\boldsymbol{\theta_I} = (\mu_I, \sigma_I) = (2.022{,}0.691)$.

S5 Instantaneous plume emission rate and wind speed uncertainty

The wind speed uncertainty $f_u(u|u_i)$ can be modelled as a Gaussian:

$$f_u(u|u_i) = \mathcal{N}(u; u_i, \sigma_u^2) = \frac{1}{\sqrt{2\pi\sigma_u^2}} e^{-\frac{(u-u_i)^2}{2\sigma_u^2}} \tag{S10}$$

And similarly for the emission rate:

$$f_q(q|q_i) = \mathcal{N}(q; q_i, \sigma_q^2). \tag{S11}$$

A reality is that the emission rate depends on the wind speed via the integrated mass enhancement (IME) equation [36]

$$q_i = \frac{IME_i \cdot U_{i;eff}}{L_i} \tag{S12}$$

Where

$$U_{i;eff} = a_0' + a_1' u_i \tag{S13}$$

And $u_i = U_{10}$ is the 10-m wind speed from the meteorological reanalysis prediction with $\{a_0', a_1'\}$ the IME equation coefficients. We could rewrite Eq. S12 as

$$q_i = a_{i;0} + a_{i,1} u_i \tag{S14}$$

With $a_{i;0} = IME_i \cdot a_0'/L_i$ and $a_{i;1} = IME_i \cdot a_1'/L_i$. There are two contributions to the instantaneous emission rate error: one from wind speed and one from identifying the IME:

$$\delta q_i^2 = \left(\frac{\partial q_i}{\partial u_i}\right)^2 (\sigma_u)^2 + \left(\frac{\partial q_i}{\partial IME_i}\right)^2 (\sigma_{IME})^2 = \left(\frac{\partial q_i}{\partial u_i}\right)^2 (\sigma_u)^2 + b^2 \tag{S15}$$

Where $b^2 = \left(\frac{\partial q_i}{\partial IME_i}\right)^2 (\sigma_{IME})^2$ is the IME error contribution.

Therefore, in the absence of wind error, we still have an emission rate error $\sigma_q^2 = b^2$. However, when there is a true wind speed u that differs from the estimated wind u_i, we can make this explicit by rewriting Eq. S14 as

$$q_i = a_{i;0} + a_{i,1} u_i = a_{i;0} + a_{i,1} u + a_{i,1}(u_i - u) = Q + a_{i,1}(u_i - u) \tag{S16}$$

Where we have made the substitution $Q = a_{i;0} + a_{i,1}u$ for the true emission rate. We can then rewrite Equation S11 as

$$f_q(Q|q_i) = \mathcal{N}\left(q; q_i, \sigma_q^2\right) = \mathcal{N}\left(q; Q + a_{i,1}(u_i - u), b^2\right). \qquad (S17)$$

S6 Posterior sampling

Posterior sampling was performed independently for each facility-year using a random-walk Metropolis-Hastings algorithm. Because the emission-state probability vector $\mathbf{p} = (p_0, \dots, p_K)$is constrained to the simplex, we represented it using an unconstrained logit vector $\boldsymbol{\theta}$ and the softmax transformation

$$p_k = \frac{\exp(\theta_k)}{\sum_{l=0}^{K} \exp(\theta_l)}. \qquad (S18)$$

The posterior probability of a candidate state was evaluated after transforming $\boldsymbol{\theta}$ to $\mathbf{p}$, using the detection-aware likelihood described in the main text together with the class-level prior. The sampler was initialized at the class-level prior distribution.

At iteration t, a candidate state was generated using an isotropic Gaussian random-walk proposal,

$$\boldsymbol{\theta}^* = \boldsymbol{\theta}^{(t)} + s\boldsymbol{\varepsilon} \qquad (S19)$$

Where $\boldsymbol{\varepsilon} \sim \mathcal{N}(\mathbf{0}, \mathbf{I})$ and s is the proposal step size. Because the proposal was symmetric, the candidate was accepted with probability

$$A = \min\left\{1, \exp\left[\ell\left(\boldsymbol{\theta}_j^*\right) - \ell\left(\boldsymbol{\theta}_j^{(t)}\right)\right]\right\}, \qquad (S20)$$

where $\ell(\boldsymbol{\theta})$denotes the log posterior evaluated using the corresponding softmax-transformed probability vector. Only differences among the logits affect $\mathbf{p}$, because the softmax transformation is invariant to addition of a common constant to all components.

Three independent chains were run for each facility-year using independently generated random seeds. Each chain comprised 2,000 burn-in iterations followed by 4,000 sampling iterations, from which every second sample was retained, yielding 2,000 retained draws per chain and 6,000 combined posterior draws per facility-year. The proposal step size was initialized at 2.0 and adapted during the first 1,000 iterations toward an acceptance rate of approximately 0.30. Retained samples from the three chains were combined to calculate posterior summaries of the emission-state probabilities, annual mean emission rate, and large-emitter persistence.

S7 Dirichlet Concentration Parameter

For each facility class, the empirical prior was defined by a class-level target distribution, $\bar{\mathbf{p}}_g$, and a concentration parameter, λ_g, that controls the degree of shrinkage toward that target. The target distribution was estimated from the pooled 2023-2025 observation histories using detection-probability-corrected counts, as described in the main text. To estimate λ_g, we first constructed provisional facility-level emission-state probability vectors, $\hat{\mathbf{p}}_j = (\hat{p}_{j0}, \dots, \hat{p}_{jK})$, for facilities with at least five valid observations. These provisional estimates used both detections and non-detections, with non-detections constraining positive emission states according to the observation-specific detection probabilities. For each emission state k, the observation-count-weighted class mean was calculated as

$$\bar{p}_{gk} = \frac{\sum_{j \in g} n_j \, \hat{p}_{jk}}{\sum_{j \in g} n_j}, \tag{S21}$$

And the between-facility variance was calculated as

$$\hat{v}_{gk} = \frac{\sum_{j \in g} n_j \left(\hat{p}_{jk} - \bar{p}_{gk}\right)^2}{\sum_{j \in g} n_j}. \tag{S22}$$

The concentration parameter was then estimated by matching this empirical variance to the marginal variance of a Dirichlet component. Using the standard approximation

$$\mathrm{Var}(p_{jk}) = \frac{\bar{p}_{gk}(1 - \bar{p}_{gk})}{\lambda_g + 1}, \tag{S23}$$

the state-specific concentration estimate is

$$\hat{\lambda}_{gk} = \frac{\bar{p}_{gk}(1 - \bar{p}_{gk})}{\hat{v}_{gk}} - 1. \tag{S24}$$

States with near-zero or near-one mean probabilities, negligible empirical variance, or non-positive concentration estimates were excluded, and the final concentration parameter was taken as the median of the remaining state-specific estimates,

$$\hat{\lambda}_g = \mathrm{median}_k(\hat{\lambda}_{gk}). \tag{S25}$$

We found values of 8.6 and 3.2 for $\hat{\lambda}_g$ for compressor/gathering stations and gas processing plants, respectively. The resulting Dirichlet parameters were defined as

$$\alpha_{gk} = 1 + \hat{\lambda}_g \bar{p}_{gk}, \qquad (S26)$$

Larger values of $\hat{\lambda}_g$ imply stronger shrinkage toward the class-level target distribution, whereas smaller values allow individual facility observation histories to exert greater influence on the posterior.

S8 Estimation Precision as a function of number of observations and detections

Figure S2 illustrates how the precision of facility-level annual emission estimates depends on the number of plume detections and total observation opportunities. Precision is summarized by

$$z = 3.92\frac{\bar{Q}}{Q_{97.5}-Q_{2.5}} \tag{S27}$$

Where $\bar{Q}$ is the mean estimate and $[Q_{2.5}, Q_{97.5}]$ the bounds of the 95% credible interval. Larger values of z indicate a narrower 95% credible interval relative to the posterior mean, and $z = 1$ corresponds to a mean being approximately one standard deviation from zero. For both compressor and gathering stations and gas processing plants, facilities with no detections generally had ($z < 1$), indicating that their uncertainty intervals were broad relative to the estimated emission rate. A single detection typically increased precision, while facilities with two or more detections generally had ($z > 1$) and progressively narrower relative uncertainty. The number of total observations had a weaker secondary influence: for a given number of detections, facilities with more observation opportunities tended to have somewhat better-constrained estimates, particularly because repeated non-detections provide additional information on the frequency of positive emission states. Nevertheless, the number of detections was the dominant predictor of estimate precision, and substantial scatter remained because precision also depends on the detected emission rates, their uncertainties, and the observation-specific probabilities of detection.

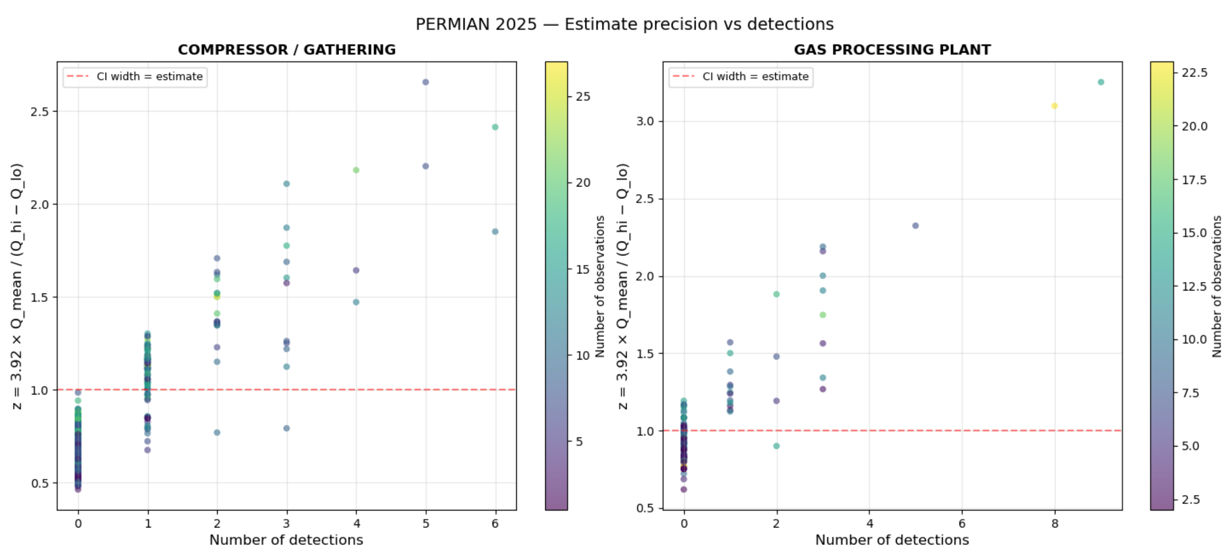

Figure S4: Emission estimate significance as a function of number of detections and observations.